Monte Carlo Simulations of Nanopore Compartmentalization Yield Fingerprint Adsorption Isotherms as a Rationale for Advanced Structure Characterization of Metal-Organic Frameworks

Shivam Parashar †, Qing Zhu^{‡, †}, Silvio Dantas †, Alexander V. Neimark ^{†, *}

[†]Department of Chemical and Biochemical Engineering, Rutgers, The State University of New Jersey, Piscataway, New Jersey 08854, United States

[‡]Department of Physics, Applied Physics, and Astronomy - Rensselaer Polytechnic Institute

*Email: aneimark@rutgers.edu

KEYWORDS: metal-organic frameworks, adsorption isotherm, pore type distribution, density profile, Monte Carlo, pore structure characterization

ABSTRACT: Unique adsorption and transport properties of metal-organic framework (MOF) materials are determined by their complex nanostructures comprised of 3D networks of pore compartments (cages, channels, windows) that differ in size, shape, and chemical functionalities. Practical MOF samples are rarely the ideal crystals: they contain binders, various defects, and

residual solvents. Reliable nanopore structure characterization methods are needed to quantify the difference between the real samples and ideal MOF crystals. Here, we construct the theoretical isotherms in individual pore compartments of MOF crystals using Monte Carlo simulations and use them as reference fingerprint isotherms. Comparison of the experimental isotherm with the theoretical fingerprint isotherms allows one to calculate the pore type distribution function, degree of sample crystallinity, adsorption capacity and accessibility of individual pore compartments. This information cannot be obtained with the currently available methods of adsorption characterization. The proposed methodology is demonstrated drawing on the examples of Ar, N₂, and CO₂ adsorption on PCN-224 and ZIF-412 MOF crystals. The constructed fingerprint isotherms are verified against the literature experimental data obtained by *in-situ* adsorption crystallography. Pore level compartmentalization of adsorption isotherms provides a better understanding of the specifics of adsorption mechanisms and distribution of adsorbed molecules between the individual pore compartments that is instrumental for the selection and design of adsorbents with improved properties for gas separations, storage, and catalysis.

1. INTRODUCTION

Metal-Organic Frameworks (MOFs) represent a wide class of crystalline nanoporous materials that are actively explored for numerous applications due to their exceptional ability to selectively adsorb, transport and retain guest molecules.¹⁻⁴ The unique abilities of MOFs stem from their tailorable porosity, record-high effective surface area, and extraordinary degree of variability of active sites.^{5,6} Significant progress has been made to understand the adsorption mechanisms,⁷⁻¹⁰ and develop advanced simulation techniques.¹⁰⁻¹⁴ In case of ideal MOF crystals, geometric properties of the crystallographic structure such as porosity, effective surface area, characteristic

pore dimensions, and pore size distribution function, can be determined by specially developed geometric methods, like Poreblazer¹⁵, and MOFomics.¹⁶ The adsorption isotherms for the ideal MOF crystals can be predicted by Monte Carlo simulations using the standard force fields and software packages, like RASPA. ¹⁷ However, practical MOF samples are rarely the ideal crystals, they contain binders, secondary structures, various defects, and residual solvents, hence their structural and adsorption properties may differ significantly from the properties of ideal crystals. It is important to devise the pore structure methods to quantify the difference of the sample morphology from the ideal crystallographic structures in terms of the degree of crystallinity, available adsorption capacity, and accessibility of active centers.

Barrett-Joyner-Halenda (BJH),¹⁸ non-local density functional theory (NLDFT),¹⁹ and quenched solid density functional theory (QSDFT)²⁰ are widely used methods to quantify the morphological properties of nanoporous materials in terms of the pore size distribution (PSD). These methods fit the experimental adsorption isotherm to the kernel of theoretical isotherms calculated in the model pores of simple shape (silt, cylindrical, or spherical) of different sizes. But these conventional methods are unable to capture the specifics of pore morphology of MOFs. MOF crystals possess a 3D pore network composed of a regular array of interconnected pore compartments, channels, and cages that differ in size, shape, and chemistry. When applied to MOF materials, the conventional methods of pore structure characterization produce the PSDs that are, in many cases, strikingly different compared to the geometric analysis of the respective crystallographic structures using the geometrical tools like Poreblazer¹⁵, and MOFomics¹⁶. Characteristic examples of such discrepancies (presented in the Supporting Information Section F) demonstrate the need for developing dedicated characterization methods that consider the specifics of pore network morphologies in MOF materials.

The non-ideality of practical MOF materials brings about additional complexity into the problem of pore structure characterization. All synthesized MOF samples contain defects to some extent. The defects may arise during the preparation method, imperfect activation of the sample, or sorption of contaminants during storage. The pores might be collapsed or blocked with nonvolatile molecules, binders, and residues. At the same time, the defects like missing linkers and nodes may produce larger pores and reduce diffusion limitations.⁴ But in general, the defects reduce the adsorption capacity and pore volume reducing the pore space accessibility. ²¹ As a result, the experimental adsorption capacity is smaller compared to the ideal crystal capacity revealed in simulations. While comparing the simulated and experimental isotherms, it is common to introduce scaling factors to match the simulated capacity with experiments.²² These scaling factors account for the inaccessible pores and nonporous inclusions without specifying their origin. It is worth noting that there were several attempts in the literature to account for the framework defects.^{23,24} For example, Janabi et al.²³ considered Cu-BTC MOF crystal and computed isotherms in several defective unit cells with blocked pockets, side pockets and principal pore compartments. By comparing the simulated adsorption isotherms in defected pores with the experimental isotherm, the authors estimated the proportion of blocked pores.²³ Recently, Krause et al.²⁵ decomposed the methane isotherm to analyze the adsorption mechanisms in the DUT family of MOFs exhibiting negative gas adsorption.

More recently, a new approach was suggested based on decomposition, or *compartmentalization* of adsorption isotherms as a sum of *fingerprint isotherms* in individual pore compartments. Applied to pore structure characterization from adsorption isotherms of reference molecular probes, the idea of compartmentalization is realized in the construction of theoretical fingerprint isotherm using molecular simulation of gas adsorption on crystallographic structures of ideal MOF

crystals.^{8, 24} Comparison of the measured isotherm of a MOF sample with a set of theoretical fingerprint isotherms allows one to construct the pore type distribution (PTD), which provides insight onto the sample structure, such as the degree of crystallinity, available porosity, and accessibility of the pore compartments of various types. Moreover, the method of fingerprint isotherms was shown to correctly predict the isosteric heat of adsorption computed from the obtained PTD for Cu-BTC sample in agreement with the experimental data.²⁴

In this work, we construct the theoretical fingerprint isotherms of Ar, N₂ and CO₂ in the pore compartments of PCN-224 and ZIF-412 MOF crystals. The choice of these systems is motivated by the availability of the experimental data presented in the pioneering study of Cho et al., ²⁶ who used the *in-situ* XRD gas adsorption crystallography for the decomposition of adsorption isotherms into sub-isotherms in the individual pore compartments. This unique work provided, for the first time in the literature, the experimental data for the verification of the simulation results. The simulated fingerprint isotherms for all adsorbates considered are found in most cases in excellent agreement with the experimental sub-isotherms²⁶. Additional justification of the proposed simulation methodology is confirmed by comparing the density distributions of adsorbates between the pore compartments with the XRD crystallography data. ²⁶ Finally, by comparing the experimental isotherms with the simulated fingerprint isotherms, the PCN-224 and ZIF-412 samples studied in ref. [26] are characterized in terms of the PTD, revealing the degree of sample crystallinity, accessibility and adsorption capacity of different pore compartments with respect to Ar, N₂ and CO₂.

2. METHODOLOGY

We performed Grand Canonical Monte Carlo (GCMC) simulations to obtain the adsorption isotherms using the open-source software package RASPA.¹⁷ A minimum of 100,000 Monte Carlo moves were attempted for equilibration and averages over at least 200,000 moves were performed for production. The probabilities for adsorbate translation, rotation, reinsertion, and swap moves were 0.2, 0.2, 0.2, and 0.4, respectively. All the isotherms were evaluated at the adsorbate normal boiling temperatures i.e., Ar (87.3 K), N₂ (77.4 K) and CO₂ (194.7 K). A simple Lennard-Jones (LJ) model was used for Ar²⁷ whereas N₂ and CO₂ were modelled as rigid multicenter molecules described by TraPPE²⁸ force field. Interaction parameters of adsorbate with framework atoms were computed using Lorentz-Berthelot mixing rules. The LJ potentials for adsorbate interactions were truncated at 17 Å for Ar and N₂, and shifted at 12 Å and 15 Å for CO₂ in PCN-224 and ZIF-412, respectively. Polarization between adsorbate and framework¹¹ was considered for CO₂ adsorption in PCN-224; the effect of CO₂ polarization on ZIF-412 was found negligible. Framework charges were obtained using the charge equilibration method²⁹ and long-range electrostatic contributions were accounted using the Ewald summation method. The PCN-224 and ZIF-412 crystallographic structures were taken from ref. [30] and [31] respectively. The forcefield parameters for C, H, N and O atoms were taken from Dreiding³² forcefield, while Zr and Zn are from UFF³³ forcefield (see Table S1 in Supporting Information, Section A). The GCMC simulation cell of PCN-224 contains one cubic unit-cell of size $38.512 \times 38.512 \times 38.512 \times m^3$ with 1216 framework atoms. From the atomic structure of the PCN-224³⁰ the central metal atom of the Tetrakis (4-carboxyphenyl) porphyrin (TCPP) ring was removed to make our structure congruent to that in the experiments.²⁶ GCMC simulations in ZIF-412 were performed on the rhombohedral shaped primitive unit cell, whose volume was 1/4th of the cubic unit cell, to reduce the computational time. The size of the simulation cell was $51.056 \times 51.056 \times 51.056$ nm³ ($\alpha, \beta, \gamma = 60^{\circ}, 60^{\circ}, 60^{\circ}$) containing 3604 framework atoms. It is worth noting that some crystallographic sites in the ZIF-412 structure file³¹ are partially occupied by multiple atoms due to an ambiguity in the distribution of some linkers: certain Imidazole, Benzimidazole, and Nitro Imidazole rings compete for the same sites (see Figure S11 in supporting information). The multiple occupancies in the structure file represents a significant challenge as they must be removed in a non-ambiguous manner. We devised a special computational procedure to generate the structures with single occupancies of atomic sites by randomly assigning the competing groups to the sites in the given proportion (see Supplementary Information, Section E).

3. RESULTS AND DISCUSSION

3.1 PCN-224

Porous Coordination Network-224 (PCN-224) is composed of Zr₆O₈ clusters interlinked by tetrakis (4-carboxyphenyl)- porphyrin (TCPP) ligands.³⁰ Figure 1 shows the cubic unit cell of the PCN-224 crystal with two types of pores: intersection pores (green) located at the body center and vertices, and channel pores (yellow) located at the edges and face centers of the cubic unit cell. The channel and intersection pores of the nominal size of 1.5 and 2.5 nm²⁶ alternate on the cubic lattice with six channel and two intersection pores per unit cell. While the porphyrin walls block the channel pores from four out of six sides, the intersection pores are unobstructed on all six sides. The unit cell was divided into compartments corresponding to individual pores as in Figure 1a. During the simulation run at a given pressure, the number of molecules in each compartment was averaged to construct the fingerprint isotherms (shown in Figure 2a).

Figure 1. (a) Crystal structure of PCN-224 showing the division of unit cells into pore compartments. (b) Intersection, and (c) channel pore. Framework atom color code: O, red; H, hidden; C, gray; N, blue; Zr, violet.

Figure 2. (a) Ar adsorption isotherm on PCN-224 obtained using GCMC simulations at 87.3 K. Fingerprint isotherms in intersection (green circles) and channel (yellow circles) pores are shown alongside with total isotherm (black circles). Closed and open circles correspond to adsorption and desorption isotherms, respectively. (b) Characteristic snapshots of the distribution of adsorbed molecules between the channel (green) and intersection (yellow) pores at different pressures from the onset of adsorption to the complete filling. Average number of molecules in each compartment is indicated below each snapshot. Vertical dashed lines in (a) indicate the pressures of the snapshots in (b). Framework atom color code: O, red; H, hidden; C, gray; N, blue; Zr, violet.

The adsorption isotherm of Argon on PCN-224 has two characteristic steps corresponding to each pore type, although, the filling of each compartment occurs in a cooperative fashion (Figure 2). The channel pore (size ~ 1.5 nm) fills continuously at low pressures, which is typical for micropores. The filling step of intersection pore (size ~ 2.5 nm) occurs stepwise via capillary condensation, as characteristic to mesopores. Figure 2b presents the snapshots of Argon in each compartment at pressures indicated by vertical lines in Figure 2a. Argon molecules are colored according to the pore they reside in, i.e., green for intersection and yellow for channel. The first $(P/P_0=7.53\times 10^{-5})$ and second $(P/P_0=0.043)$ snapshots correspond to the onset of adsorption in the channel and intersection pore, respectively whereas the third $(P/P_0 = 0.129)$ and fourth $(P/P_0 = 0.151)$ snapshots show the filled channel and intersection pores, respectively. The simulated and experimental isotherm of Ar on PCN-224 are compared in Figure 3a. Simulated isotherms correspond to the ideal crystal with all pores completely accessible for the adsorbate. To match the simulated isotherms with the experimental data we scale down the fingerprint isotherms in the channel and intersection pores by the accessibility factors of 0.58 and 0.62, respectively (Figure 3a). The scaled simulated isotherms are found in excellent agreement with the experiments in the whole range of the gas pressure. This agreement suggests that the crystallinity of the PCN-224 sample used for Ar measurements was ~60%, or that the accessible pore volumes of channel and intersection pores constituted ~58% and 62% of the respective pore volumes in the ideal crystal of the same weight as the sample.

Figure 3. Comparison of experimental²⁶ (squares) and simulated adsorption isotherms (circles) of (a) Ar at 87.3 K, (b) N₂ at 77.4 K and (c) CO₂ at 194.7 K on PCN-224. The closed and open circles correspond to adsorption and desorption isotherms, respectively. Fingerprint isotherms in channel and intersection pores are plotted in yellow and green, respectively. (a) Simulated fingerprint isotherms are scaled down by the accessibility factors of 0.58 and 0.62 for channel and intersection pore for Ar; (b) 0.63 and 0.65 for N₂; (c) 0.66 and 0.70 for CO₂ to match the experimental total capacity of each pore which is indicated by horizontal dashed lines.

Figure 3b and 3c presents the comparison between the total experimental and simulated isotherms of N_2 at 77.4 K and CO_2 at 194.7 K. Since the experimental sub-isotherms are not available for N_2 and CO_2 , we scale the fingerprints isotherms to match the experimental density²⁶ at saturation for individual pores (indicated by dashed lines). For N_2 , the channel and intersection pore fingerprint isotherms are rescaled by 0.63 and 0.65, respectively. As expected, N_2 adsorption at 77 K (Figure 3a) occurs in a similar fashion as Ar at 87 K: the fingerprint isotherm for the intersection compartment has a stepwise behavior, with pore filling occurring at $\sim 0.13 \, P/P_0$, while the channel pores are filled gradually. The total isotherm (black circles) represents the sum of scaled fingerprint isotherm and agrees well with the experimental data (red squares) in the whole range of the gas pressure.

The CO₂ isotherms on PCN-224 are presented in Figure 3c. We also included the polarization potential between the framework atoms and CO₂ molecules according to the prescription in ref. ¹¹ Like the Ar and N₂ isotherms, we match the experimental adsorption capacities of individual pores (shown by dashed lines) by rescaling the CO₂ fingerprint isotherms in channel and intersection pores by 0.66 and 0.70, respectively. CO₂ at 195 K fills the pores at higher pressures and in a

broader range than Ar at 87 K and N_2 at 77 K because of higher temperature of adsorption. Filling of the intersection pores with CO_2 starts when the channel pores are almost filled. The intersection pores are filled abruptly at $P/P_0 = 0.42$ and desorption occurs at lower pressures demonstrating a small H1-type hysteresis. It is worth noting, the polarization effects in PCN-224 are found very significant, especially at low pressures. Neglect of polarization leads to underprediction of adsorption compared to the experiments (see Supporting Information, Section A).

It is worth noting that adsorption and desorption isotherms simulated by GCMC commonly exhibit hysteresis in small mesopores of 2-4 nm, which is not observed in the experiments. 34-36 This behavior is found for CO₂ adsorption in PCN-224 intersection pores of size ~2.5 nm. The adsorption hysteresis is related with the existence of metastable states of confined fluid, which are separated from the equilibrium states by energy barriers. Due to a limited simulation time and absence of natural fluctuations of external conditions, the probability of crossing the energy barriers in simulations is by orders of magnitude smaller than in the experiments. The larger the pore and the low the temperature, the higher the energy barriers. It was shown that in mesoporous materials, adsorption hysteresis at normal boiling temperatures is observed experimentally only in pores larger ~4-5 nm, while in simulations, hysteresis is inherent for pores larger than 2 nm. 36 Our simulations of adsorption in PCN-224, as well as in ZIF-412 confirm this conclusion.

Figure 4 shows the simulated and experimental density profiles of Ar in channel and intersection pores at different pressures. The densities are presented along lateral and diagonal directions. The simulated densities were scaled down by 0.7 to match the experimental density at saturation. The evolution of adsorbate densities as the pressure increases confirms that the channel pores are filled continuously. For $P/P_0 = 0.11$ (cyan), the intersection pore is empty while the channel pore is almost filled. A sudden increase of the density in the intersection pores from $P/P_0 = 0.11$ (cyan)

to $P/P_0 = 0.16$ (blue) indicates the intersection pore filling due to capillary condensation. In the channel pores, the density along the lateral direction (x, 1-x, 0.5) is larger compared to diagonal (0, y, 0.5) for the same pressure, due to the enhanced attractive potential created by the framework atoms along the diagonal direction. The simulated density profiles agree well with experimental data. Such detailed agreement confirms the validity of our simulation methodology.

Figure 4. (a) Schematic of PCN-224 unit cell showing the directions along which the density profiles of Argon are computed: along (0, y, 0.5) and (x, 1-x, 0.5) (b) simulated, and (c) experimental²⁶ density profiles. Simulated densities are multiplied by the factor of 0.7 to match the experimental densities.

3.2 ZIF-412

Zeolitic Imidazolate Framework-412 (ZIF-412) framework is composed of Zn atoms bonded together with three types of linkers: Imidazole, benzene Imidazole, and nitro Imidazole rings. ZIF-412 represents a mesoporous material with the pore network composed by three types of cage-like compartments connected by narrower windows. Figure 5a shows the pore arrangement in the cubic unit cell of the ZIF-412 crystal: lta (Linde Type A) cages in orange are located on the face centers

and vertices, fau (Faujasite) cages in green on the cube diagonals close to the vertices, and ucb³¹ cages (yellow) in the cell center and at the edges (ucb cages at the unit cell edges are not shown for the sake of clarity). The lta pore is the smallest of the three pores with the geometric diameter of 2.1 nm. Six narrow 0.8 nm windows connect lta pores to the ucb cages of size 3.9 nm. Each ucb cage is connected to eight fau cages of size 2.5 nm. The pore window between ucb and fau cages is 1.5 nm wide. We divide the unit cell into the pore compartments (Figure 5b) and count the average number of molecules in each compartment to construct the fingerprint isotherm.

Figure 5. (a) Crystal structure of ZIF-412 showing the location of pores within a unit cell. (b) Division of unit cell into pore compartments. (c), (d), (e) are the structure of lta, fau and ucb cages respectively for which the pore volume is represented by a sphere. Framework atom color code; O: Red, H: Hidden, C: Gray, N: Blue, Zn: Green.

The simulated Ar isotherms on ZIF-412 are shown in Figure 6 in comparison with the experimental data²⁶. The GCMC isotherm in Figure 6d has a H1 type hysteresis loop typical for capillary condensation in mesoporous solid. However, the shape of the isotherm prior to the condensation transition is more convex compared to the multilayer adsorption isotherm usually observed for mesoporous materials. The experimental isotherm has a similar shape as the simulated isotherm with three main distinctions. Firstly, the experimental isotherm is reversible that is common for mesoporous materials with pores smaller than 4 nm; the absence of hysteresis

is explained by low nucleation barriers of capillary condensation that can be overcome due to natural thermal fluctuations in the experiments but are prohibitive in MC simulations. Secondly, the experimental capillary condensation takes place at a higher vapor pressure that in MC simulations. This discrepancy could not be improved by forcefield adjustment within reasonable limits. Possible reasons for this discrepancy are discussed in the Supplementary Information, Section B and C. In particular, we show that increase of simulation temperature to 90 K gives good correspondence with experiments. Thirdly, the experimental adsorption capacity is ~90 % of the simulations indicating that either the sample has non-porous inclusions, or a significant portion of pores is blocked and inaccessible. The answer to this question is revealed by the analysis of the fingerprint isotherms.

Figure 6: Comparison of experimental (squares) and theoretical fingerprint isotherms (circles) of Ar in (a) Ita, (b) fau, (c) ucb cage and (d) total isotherms. The closed and open circle correspond to adsorption and desorption isotherms, respectively. The red circles in fingerprint isotherms correspond to the snapshots showing the sequence of adsorption. Average number of molecules adsorbed in each pore is printed below each snapshot.

The fingerprint isotherms shed light on the specifics of adsorption mechanisms due to the morphological complexity of ZIF-412 pore structure comprised of three distinct pore compartments. The fingerprint isotherms of Ar adsorption in lta, fau, and ucb cages are shown in Figure 6a, b, c. We observe that Ita pores are gradually filled achieving the complete capacity at $\sim 0.03 \ P/P_0$. Filling of fau cages is associated with a sharper reversible step at ~ 0.02 -0.05 P/P_0 . In contrast, adsorption in ucb cages exhibits a capillary condensation – desorption hysteresis loop at ~ 0.18 -0.27 P/P_0 . The simulated isotherms correspond to the ideal crystal with all pores fully accessible due to which fingerprint isotherms (circles) predict larger adsorption compared to experimental sub-isotherms. It is worth noting that the sub-isotherms²⁶ are determined from the XRD measurements; they start from higher pressures $(P/P_0 \sim 10^{-2})$ and contain fewer point than the total isotherm measured volumetrically. The lta fingerprint isotherm have the largest difference in the saturation capacity compared to the experimental sub-isotherm (Figure 6a). This suggests that a significant portion of lta pores is inaccessible in the experimentally studied crystal. Indeed, as seen in Figure 7a, scaling down the lta fingerprint isotherm by the accessibility factor of 0.54 results in a good match with the experimental sub-isotherm determined by in situ XRD crystallography. At the same time, the theoretical adsorption capacities of fau and ucb cages are close the experimental that suggests minor blockage of these pore compartments. To match the experimental data, the fingerprint isotherms fau and ucb cages were scaled down by the accessibility factors of 0.95 and 0.98, respectively (Figure 7a).

Figure 7. Comparison of experimental²⁶ (squares) and simulated adsorption isotherms (circles) of (a) Ar at 87.3 K, (b) N_2 at 77.4 K, and (b) CO_2 at 194.7 K on ZIF-412. The open and closed circles correspond to adsorption and desorption isotherms, respectively. For Ar, the accessibility factors for lta, fau, and ucb cages are 0.54, 0.95, and 0.98 respectively whereas for N_2 , only the fingerprint isotherm in lta cage is multiplied by the accessibility factor of 0.58 to match the experimental²⁶ pore capacities (horizontal dashed lines). For CO_2 , all accessibility factors are equal to 1.

Figure 7b, c presents the comparison between the total simulated and experimental isotherm of N_2 at 77.4 K and CO_2 at 194.7 K. For N_2 , the accessibility factors are 0.58, 1, and 1 for Ita, fau, and ucb pores respectively indicating that only 58 % of the Ita pores were accessible in the experimentally studied sample whereas all fau and ucb pore were fully accessible. The total isotherm (black circles) is the sum of scaled fingerprint isotherm which agrees well with experimental data (red squares). The overall pore filling behavior of N_2 at 77 K is very similar to Ar- Ita pores filling before ~ 0.03 P/P₀, fau between ~ 0.02 -0.05 P/P₀ and ucb at slightly higher relative pressures ~ 0.22 -0.27. N_2 also exhibits a hysteresis but smaller compared to Ar (Figure 7a).

For CO₂ (Figure 7b), the accessibility factors for lta, fau and ucb cages are equal to one suggesting that all pores were completely accessible to CO₂ in the experimental sample. This may be due to its smaller kinetic diameter and higher temperature (194.7 K) compared to Ar (87.3 K) and N₂ (77.4 K). The agreement between the total simulated and experimental isotherm is accurate, except that the simulated isotherms exhibit a wide hysteresis in the ucb cage whereas experimental

isotherm is reversible. The hysteresis loop is widest for CO_2 in comparison to Ar and N_2 because the adsorption temperature of CO_2 (194.7 K) is well below the triple point (216.6 K). Hysteretic behavior in our simulations is due to formation of a metastable state and lower thermal fluctuations which would disappear for an infinitely long simulation.^{37,38}

We computed the density profiles of CO_2 along three directions connecting Ita, fau and ucb pores diagonally, Ita and ucb cages laterally, and two fau cages laterally as shown in Figure 8a. Simulated density profiles (Figure 8b) confirm that the Ita pore gets filled before $P/P_0 \sim 0.197$ (orange), fau between $P/P_0 \sim 0.326-0.444$ and ucb below $P/P_0 \sim 0.790$. Compared to experimental density profile (Figure 8c) the simulated profiled are in a good qualitative and quantitative agreement.

Figure 8. (a) Schematic of ZIF-412 structure showing the directions - (x, x, x), (0.5, y, 0), and (0.25, y, 0.25) along which the density profile of CO₂ was computed at various pressures. (b) Simulated, and (c) Experimental²⁶ density profiles in each of those directions.

3.3 PORE TYPE DISTRIBUTION

The fingerprint isotherms allow to analyze to what extent the pore structure of a given MOF sample is similar (or different) to the pore structure of the ideal crystal and calculate the pore type distribution (PTD). To this end, the experimental isotherm, N_{exp} , is presented as a weighed sum of the fingerprint isotherms, N_i^{FP} ,

$$N_{\rm exp} = \sum_{i} \varphi_i N_i^{FP},\tag{1}$$

The weights φ_i represent the contributions of the individual pore compartments into the total adsorption and represent the accessibility factors, which quantify the deviations of the sample structure from the ideal crystal.

For the PCN-224 and ZIF-412 samples considered here, the PTD is presented as the histogram of the volumes of individual pores accessible for given adsorbate per unit mass of the sample (Figure 9). Here, the pore volumes are defined not from their geometry in the crystallographic structure but from the adsorption capacities using the Gurvich rule³⁹ by dividing the adsorption at saturation ($P/P_0 \rightarrow 1$) in mol/g by the bulk fluid density in cc/mol.⁴⁰ This is why the pore volumes determined by different adsorbates may differ. The accessibility factors φ_i characterize the ratio of the accessible volume of given pore compartment in the sample to the compartment volume in the ideal crystal. The hollow transparent bars in Figure 9 represent the pore volumes of the individual pores accessible for Ar, N₂ and CO₂ in the ideal crystal, and the filled bars represent the respective pore volumes determined from the experimental isotherms. The percentage (φ_i *

100 %) of pore volume available in experiments compared to ideal volume available in simulations is indicated on each bar.

For PCN-224 sample (Figure 9a), the channel and intersection pores are almost equally available: \sim 60 % for argon adsorption, \sim 64 % for N_2 and \sim 68 % for CO_2 . This suggests that the crystallinity of the sample (in terms of the ratio of the mass of the crystal phase to the sample mass) is about \sim 64 +/-4 %. For ZIF-412 sample (Figure 9b), CO_2 adsorption indicates the sample is close to the ideal crystal, as the experimental accessibility of all three pore compartments is \sim 100%. However, while the fau and ucb cages are also almost fully accessible for Ar and N_2 , the smallest Ita pores are only partially accessible by (\sim 53 % and \sim 58 %) by these adsorbates. The explanation why the Ita pores are fully accessible for CO_2 but only partially for Ar and N_2 , deserve further analysis of the specifics of the ZIF-412 structure. For both MOFs samples, the volume accessed by different adsorbates follows this order: $CO_2 > N_2 > Ar$. CO_2 accessed all pores in ZIF-412 because of its smaller size and higher adsorption temperature of CO_2 (194.7 K) compared to Argon (87.3 K) and N_2 (77.4 K).

In the above analysis of PTD in the PCN-224 and ZIF-412 samples, we took advantage of the availability of the experimental sub-isotherms in individual pore compartments. Based on the standard measurements of the total adsorption isotherm, the PTD can be determined by fitting the accessibility factors φ_i of the simulated fingerprint isotherms, N_i^{FP} , in eq. 1 to reproduce the experimental isotherm, N_{exp} .

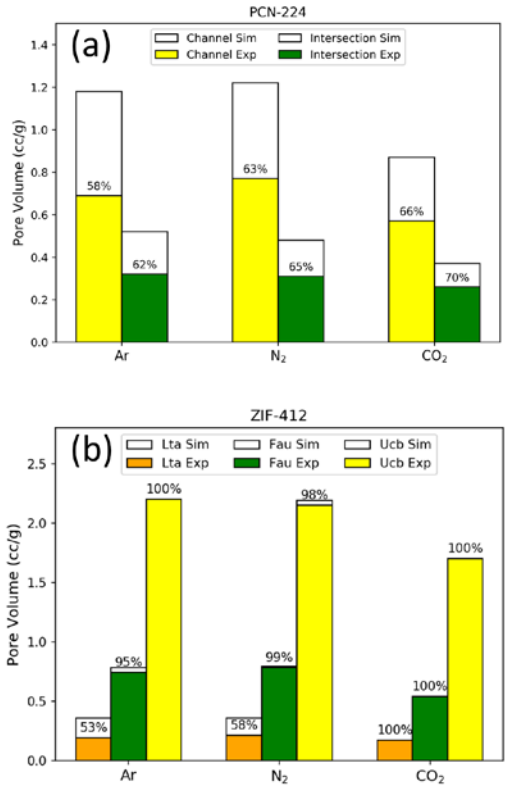


Figure 9. Pore type distribution in (a) PCN-224 and (b) ZIF-412 calculated for Ar, N_2 and CO_2 . The empty bars represent the simulated pore volume of each pore type while the filled colored bars are experimental pore volumes. The accessibility factors (in percentage) are printed on the top of the bars.

4. CONCLUSION

To what extent the nanopore structure of synthesized samples of MOF materials is different from the structure of ideal crystals? This question is one of the most important for the design and selection of novel MOF structures for practical applications. Samples of MOF materials rarely represent ideal crystals and, in most cases, contain non-crystalline inclusions, binders, residual chemicals, and various types of defects. The cages and channels of varied sizes, shapes, and chemistries, which comprise the 3D pore network, may be completely or partially blocked, thus

reducing the pore accessibility and adsorption capacity. The method of fingerprint isotherms, proposed by us recently, ²⁴ allows to assess the degree of sample crystallinity, adsorption capacities and accessibilities of different pore compartments from the experimental adsorption isotherms. The method is based on the construction by MC simulation the theoretical adsorption isotherm that is divided into a set of reference fingerprint isotherms in individual pore compartments of the ideal crystallographic structure. The pore accessibilities are calculated as the weights in the representation of the experimental isotherm as a weighted sum of fingerprint isotherms. The results are presented in terms of the pore type distribution (PTD) that determines the volume fractions of pores of different types in the sample under study.

The method of fingerprint isotherms is illustrated and validated on drawing on the examples of adsorption of Ar, N₂ and CO₂ adsorption at the respective normal boiling temperatures on PCN-224 and ZIF-412 MOF materials. This choice is motivated by the availability of the unique data of *in-situ* adsorption XRD crystallography that for the first time allowed for identification of measured adsorption in different pore compartments, construction of respective sub-isotherms and 3D adsorbate density distribution in the pore system at varying gas pressure.²⁶ We found good agreement between the simulated and experimental data not only on the isotherms measured by crystallography and volumetrically, but also on the adsorbate density profiles in different crystallographic directions. The latter comparison is most instructive and reveals the detailed adsorption and pore filling mechanisms. The calculated PTD and accessibility factors made it possible to make conclusions about the quality of the samples considered. By comparing the fingerprint isotherms with the experiments, one evaluates the accessibility factors of individual pore compartments for a given adsorbate. The accessibility factors depend on the degree of crystallinity (fraction of crystalline phase in the sample) and on the compartment accessibilities

within the crystal. The degree of crystallinity may be determined by an expert estimate, as the largest accessibility factor among all pore compartments for a given adsorbate. In case of ZIF-412, the degree of crystallinity is ~100% with ucb and fau pores practically fully available to all adsorbates, and lta pores fully available for CO₂ and only partially for Ar and N₂. In case of PCN-224, the accessibility factors vary between 58 and 70%, and it is safe to conclude the crystallinity factor of not larger than 70%, assuming that the channel pores in the crystalline phase are fully available to CO₂. These examples show that the method of fingerprint isotherms provides a better understanding of the specifics of adsorption mechanisms and distribution of adsorbed molecules between the individual nanopore compartments that is instrumental for the selection and design of novel adsorbents with improved properties for gas separations, storage, and catalysis.

Our calculations confirm the importance of the polarization effect for CO₂ adsorption on MOFs. The difference between the simulations with and without the polarization potential between CO₂ and PCN-224 framework is found very significant (see Figure S1). Neglect of polarization effect causes a shift of the adsorption isotherms to higher pressures compared with the experimental isotherm. At the same time, the polarization effect for CO₂ adsorption on ZIF-412 is found insignificant.

The method of fingerprint isotherms can be extended to other families of MOF materials, as the crystallographic structures are available in different databases^{41, 42} and theoretical fingerprint isotherms can be calculated using standard forcefields (UFF, Dreiding, etc) with MC simulation software package like RASPA.¹⁷ However, while the MC simulation of adsorption isotherms is considered as a routine, there are certain challenges that must be critically evaluated and analyzed. Some of these issues, that we encountered in the systems studied here, are discussed in the text and in the Supplementary Information. The division of the pore space into individual pore

compartments, that is in many systems obvious, for some structures may be ambiguous due to the pore intersections that can be attributed to either of neighboring pores. MOFs with different types of linkers, such as ZIF-412, can contain fractional occupancies in their crystallographic structures and must be treated prior to adsorption modeling. For the adjustment of structures with fractional occupancies, we devised a computational procedure that can be employed for other structures (see supporting information, section E). It is very important to visualize the structure carefully (to check for partial occupancies of atoms) and clean it before performing GCMC simulations. Removal of partial occupancies using our algorithm gives not one but a collection of true structures that differ in the relative positioning of the linkers. Another important complication arises from different degrees of hydration and non-uniform distribution of residual chemicals in practical samples that not only alter the adsorption space and pore dimensions, but also affect the adsorption interactions. It is worth noting, that as shown in the presented examples, the pore structure characteristics determined from adsorption of different adsorbate may differ. In this respect, CO₂ has certain advantages as a molecular probe, compared to N2 and Ar due to its higher mobility and capability of penetrating into the smallest micropores.

The proposed methodology can be extended further to evaluate the nanopores within secondary binder phase and defected pores within the crystal phase of MOF materials by combining the kernel of fingerprint isotherms with a conventional kernel of theoretical isotherms obtained by NLDFT or QSDFT methods.⁴³ Such hybrid kernel will allow to determine the accessibilities of intact pore compartments in the crystal phase and the effective size distribution of the binder and defective pores.

Supporting Information with simulation details, density profile calculation, dependence of isotherm on the truncation of potential, pore volumes, partial occupancies in ZIF-412 (file type, PDF).

AUTHOR INFORMATION

Corresponding Author

Alexander V. Neimark – Department of Chemical and Biochemical Engineering, Rutgers, The State University of New Jersey, Piscataway, New Jersey 08854, United States; orcid.org/0000-0002-3443-0389; Email: aneimark@rutgers.edu

Author Contributions

All authors have given approval to the final version of the manuscript.

Funding Sources

This work is supported by the National Science Foundation (CBET grant no. 1834339)

ACKNOWLEDGEMENT

Author expresses a huge thanks to Filip Formalik and Peter Ravikovitch for useful discussions.

REFERENCES

1. Zhou, H.-C.; R. Long, J.; M. Yaghi, O., Introduction to Metal-Organic Frameworks. *Chemical Reviews* **2012**, *112* (2), 673-674.

- 2. Pascanu, V.; Miera, G. G.; Inge, A. K.; Martin-Matute, B., Metal-Organic Frameworks as Catalysts for Organic Synthesis: A Critical Perspective. *Journal of the American Chemical Society* **2019**, *141* (18), 7223-7234.
- 3. Sturluson, A.; Huynh, M. T.; Kaija, A. R.; Laird, C.; Yoon, S.; Hou, F.; Feng, Z. X.; Wilmer, C. E.; Colon, Y. J.; Chung, Y. G.; Siderius, D. W.; Simon, C. M., The role of molecular modelling and simulation in the discovery and deployment of metal-organic frameworks for gas storage and separation(dagger). *Molecular Simulation* **2019**, *45* (14-15), 1082-1121.
- 4. Xiang, W.; Zhang, Y.; Chen, Y.; Liu, C.-j.; Tu, X., Synthesis, characterization and application of defective metal–organic frameworks: current status and perspectives. *Journal of Materials Chemistry A* **2020**, *8* (41), 21526-21546.
- 5. Cohen, S. M., Postsynthetic Methods for the Functionalization of Metal-Organic Frameworks. *Chemical Reviews* **2012**, *112* (2), 970-1000.
- 6. Yuan, S.; Feng, L.; Wang, K.; Pang, J.; Bosch, M.; Lollar, C.; Sun, Y.; Qin, J.; Yang, X.; Zhang, P.; Wang, Q.; Zou, L.; Zhang, Y.; Zhang, L.; Fang, Y.; Li, J.; Zhou, H.-C., Stable Metal-Organic Frameworks: Design, Synthesis, and Applications. *Advanced Materials* **2018**, *30* (37), 1704303.
- 7. Cychosz Struckhoff, K.; Thommes, M.; Sarkisov, L., On the Universality of Capillary Condensation and Adsorption Hysteresis Phenomena in Ordered and Crystalline Mesoporous Materials. *Advanced Materials Interfaces* **2020**, *7* (12), 2000184.
- 8. Dantas, S.; Sarkisov, L.; Neimark, A. V., Deciphering the Relations between Pore Structure and Adsorption Behavior in Metal-Organic Frameworks: Unexpected Lessons from

Argon Adsorption on Copper–Benzene-1,3,5-tricarboxylate. *Journal of the American Chemical Society* **2019**, *141* (21), 8397-8401.

- 9. Park, J.; Howe, J. D.; Sholl, D. S., How Reproducible Are Isotherm Measurements in Metal–Organic Frameworks? *Chemistry of Materials* **2017**, *29* (24), 10487-10495.
- 10. Walton, K. S.; Millward, A. R.; Dubbeldam, D.; Frost, H.; Low, J. J.; Yaghi, O. M.; Snurr, R. Q., Understanding inflections and steps in carbon dioxide adsorption isotherms in metalorganic frameworks. *J Am Chem Soc* **2008**, *130* (2), 406-7.
- 11. Becker, T. M.; Dubbeldam, D.; Lin, L.-C.; Vlugt, T. J. H., Investigating polarization effects of CO2 adsorption in MgMOF-74. *Journal of Computational Science* **2016**, *15*, 86-94.
- 12. Jablonka, K. M.; Ongari, D.; Smit, B., Applicability of Tail Corrections in the Molecular Simulations of Porous Materials. *Journal of Chemical Theory and Computation* **2019**, *15* (10), 5635-5641.
- 13. Ongari, D.; Boyd, P. G.; Kadioglu, O.; Mace, A. K.; Keskin, S.; Smit, B., Evaluating Charge Equilibration Methods To Generate Electrostatic Fields in Nanoporous Materials. *J Chem Theory Comput* **2019**, *15* (1), 382-401.
- 14. Zhang, K.; Nalaparaju, A.; Chen, Y. F.; Jiang, J. W., Crucial role of blocking inaccessible cages in the simulation of gas adsorption in a paddle-wheel metal-organic framework. *Rsc Advances* **2013**, *3* (36), 16152-16158.
- 15. Sarkisov, L.; Harrison, A., Computational structure characterisation tools in application to ordered and disordered porous materials. *Molecular Simulation* **2011**, *37* (15), 1248-1257.

- 16. First, E. L.; Floudas, C. A., MOFomics: Computational pore characterization of metalorganic frameworks. *Microporous and Mesoporous Materials* **2013**, *165*, 32-39.
- 17. Dubbeldam, D.; Calero, S.; Ellis, D. E.; Snurr, R. Q., RASPA: Molecular simulation software for adsorption and diffusion in flexible nanoporous materials. *Molecular Simulation* **2016**, *42* (2), 81-101.
- 18. Barrett, E. P.; Joyner, L. G.; Halenda, P. P., The Determination of Pore Volume and Area Distributions in Porous Substances. I. Computations from Nitrogen Isotherms. *Journal of the American Chemical Society* **1951**, *73* (1), 373-380.
- 19. Lastoskie, C.; Gubbins, K. E.; Quirke, N., Pore size distribution analysis of microporous carbons: a density functional theory approach. *The Journal of Physical Chemistry* **1993**, *97* (18), 4786-4796.
- 20. Ravikovitch, P. I.; Neimark, A. V., Density Functional Theory Model of Adsorption on Amorphous and Microporous Silica Materials. *Langmuir* **2006**, *22* (26), 11171-11179.
- 21. Moellmer, J.; Celer, E. B.; Luebke, R.; Cairns, A. J.; Staudt, R.; Eddaoudi, M.; Thommes, M., Insights on Adsorption Characterization of Metal-Organic Frameworks: A Benchmark Study on the Novel soc-MOF. *Microporous and Mesoporous Materials* **2010**, *129* (3), 345-353.
- 22. Chowdhury, P.; Bikkina, C.; Meister, D.; Dreisbach, F.; Gumma, S., Comparison of adsorption isotherms on Cu-BTC metal organic frameworks synthesized from different routes. *Microporous and Mesoporous Materials* **2009**, *117* (1), 406-413.

- 23. Al-Janabi, N.; Fan, X.; Siperstein, F. R., Assessment of MOF's Quality: Quantifying Defect Content in Crystalline Porous Materials. *J Phys Chem Lett* **2016**, 7 (8), 1490-4.
- 24. Dantas, S.; Neimark, A. V., Coupling Structural and Adsorption Properties of Metal-Organic Frameworks: From Pore Size Distribution to Pore Type Distribution. *Acs Appl Mater Inter* **2020**, *12* (13), 15595-15605.
- 25. Krause, S.; Evans, J. D.; Bon, V.; Senkovska, I.; Iacomi, P.; Kolbe, F.; Ehrling, S.; Troschke, E.; Getzschmann, J.; Többens, D. M.; Franz, A.; Wallacher, D.; Yot, P. G.; Maurin, G.; Brunner, E.; Llewellyn, P. L.; Coudert, F.-X.; Kaskel, S., Towards general network architecture design criteria for negative gas adsorption transitions in ultraporous frameworks. *Nature Communications* **2019**, *10* (1), 3632.
- 26. Cho, H. S.; Yang, J.; Gong, X.; Zhang, Y. B.; Momma, K.; Weckhuysen, B. M.; Deng, H.; Kang, J. K.; Yaghi, O. M.; Terasaki, O., Isotherms of individual pores by gas adsorption crystallography. *Nat Chem* **2019**, *11* (6), 562-570.
- 27. Rowley, L. A.; Nicholson, D.; Parsonage, N. G., Monte Carlo grand canonical ensemble calculation in a gas-liquid transition region for 12-6 Argon. *Journal of Computational Physics* **1975**, *17* (4), 401-414.
- 28. Potoff, J. J.; Siepmann, J. I., Vapor–liquid equilibria of mixtures containing alkanes, carbon dioxide, and nitrogen. *AIChE Journal* **2001**, *47* (7), 1676-1682.
- 29. Rappe, A. K.; Goddard, W. A., Charge equilibration for molecular dynamics simulations. *The Journal of Physical Chemistry* **1991**, *95* (8), 3358-3363.

- 30. Feng, D.; Chung, W. C.; Wei, Z.; Gu, Z. Y.; Jiang, H. L.; Chen, Y. P.; Darensbourg, D. J.; Zhou, H. C., Construction of ultrastable porphyrin Zr metal-organic frameworks through linker elimination. *Journal of the American Chemical Society* **2013**, *135* (45), 17105-17110.
- 31. Yang, J.; Zhang, Y. B.; Liu, Q.; Trickett, C. A.; Gutierrez-Puebla, E.; Monge, M. A.; Cong, H.; Aldossary, A.; Deng, H.; Yaghi, O. M., Principles of Designing Extra-Large Pore Openings and Cages in Zeolitic Imidazolate Frameworks. *J Am Chem Soc* **2017**, *139* (18), 6448-6455.
- 32. Mayo, S. L.; Olafson, B. D.; Goddard, W. A., Dreiding a Generic Force-Field for Molecular Simulations. *J Phys Chem-Us* **1990**, *94* (26), 8897-8909.
- 33. Rappe, A. K.; Casewit, C. J.; Colwell, K. S.; Goddard, W. A.; Skiff, W. M., Uff, a Full Periodic-Table Force-Field for Molecular Mechanics and Molecular-Dynamics Simulations. *Journal of the American Chemical Society* **1992**, *114* (25), 10024-10035.
- 34. Dantas, S.; Struckhoff, K. C.; Thommes, M.; Neimark, A. V., Phase Behavior and Capillary Condensation Hysteresis of Carbon Dioxide in Mesopores. *Langmuir* **2019**, *35* (35), 11291-11298.
- 35. Neimark, A. V.; Vishnyakov, A., Phase Transitions and Criticality in Small Systems: Vapor–Liquid Transition in Nanoscale Spherical Cavities. *The Journal of Physical Chemistry B* **2006**, *110* (19), 9403-9412.
- 36. Neimark, A. V.; Ravikovitch, P. I.; Vishnyakov, A., Adsorption hysteresis in nanopores. *Phys Rev E Stat Phys Plasmas Fluids Relat Interdiscip Topics* **2000**, *62* (2 Pt A), R1493-6.

- 37. Schoen, M.; Rhykerd, C. L.; Cushman, J. H.; Diestler, D. J., Slit-pore sorption isotherms by the grand-canonical Monte Carlo method. *Molecular Physics* **2006**, *66* (6), 1171-1182.
- 38. Sarkisov, L.; Monson, P. A., Hysteresis in Monte Carlo and Molecular Dynamics Simulations of Adsorption in Porous Materials. *Langmuir* **2000**, *16* (25), 9857-9860.
- 39. Rouquerol, F. o.; Rouquerol, J.; Sing, K. S.; Llewellyn, P.; Maurin, G., Adsorption by powders and porous solids: principles, methodology and applications. 2014.
- 40. Lemmon, E. W.; McLinden, M. O.; Friend, D. G., Thermophysical Properties of Fluid Systems. In NIST Chemistry WebBook, NIST Standard Reference Database Number 69, Eds. P.J. Linstrom and W.G. Mallard, National Institute of Standards and Technology, Gaithersburg MD, 20899.
- 41. Chung, Y. G.; Camp, J.; Haranczyk, M.; Sikora, B. J.; Bury, W.; Krungleviciute, V.; Yildirim, T.; Farha, O. K.; Sholl, D. S.; Snurr, R. Q., Computation-Ready, Experimental Metal—Organic Frameworks: A Tool To Enable High-Throughput Screening of Nanoporous Crystals. *Chemistry of Materials* **2014**, *26* (21), 6185-6192.
- 42. Groom, C. R.; Bruno, I. J.; Lightfoot, M. P.; Ward, S. C., The Cambridge Structural Database. *Acta Crystallographica Section B* **2016**, *72* (2), 171-179.
- 43. Landers, J.; Gor, G. Y.; Neimark, A. V., Density functional theory methods for characterization of porous materials. *Colloids and Surfaces A: Physicochemical and Engineering Aspects* **2013**, *437*, 3-32.

Insert Table of Contents artwork here

